Damage analysis of composite–aluminium adhesively-bonded single-lap joints

Damage analysis of composite-aluminium adhesively-bonded single-lap joints

T.E.A. Ribeiro[*], R.D.S.G. Campilho[*1], L.F.M. da Silva[**], L. Goglio[***]

* Departamento de Engenharia Mecânica, Instituto Superior de Engenharia do Porto, Instituto Politécnico do Porto, Rua Dr. António Bernardino de Almeida, 431, 4200-072 Porto, Portugal

** Departamento de Engenharia Mecânica, Faculdade de Engenharia da Universidade do Porto Rua Dr. Roberto Frias, s/n, 4200-465 Porto, Portugal

*** Department of Mechanical and Aerospace Engineering, Politecnico di Torino, corso Duca degli Abruzzi 24, 10124 Torino, Italia

Abstract

Adhesive bonding is a permanent process that uses an adhesive to bond the components of a structure. This bonding process is used to fabricate structures of complex shape that could not be manufactured in one piece, to provide a structural bond that ideally should be at least as resistant as the base materials. Composite materials reinforced with fibres are becoming increasingly popular in many applications as a result of a number of competitive advantages. In the manufacture of composite structures, although the fabrication techniques reduce to the minimum the connections by means of advanced manufacturing techniques, the use of connections is still required due to the typical size limitations and design, technological and logistical aspects. Moreover, it is known that in many high performance structures, joints between composite materials with other light metals such as aluminium are required, for purposes of structural optimization. This work addresses numerically and experimentally adhesive joints between aluminium and carbon-epoxy composite components, considering different adhesives and geometric conditions. The strength and failure modes are studied, optimizing the geometry and material parameters of the joints. Numerically, the Finite Element Method (FEM) is used to perform detailed stress and damage analyses allowing to explain the joints behaviour. The use of cohesive zone models (CZM) enables predicting the joint strength and creating a simple and rapid design methodology. The joints' strength and failure modes were highly dependent on the adhesive, and this behaviour was successfully modelled numerically.

Keywords: Hybrid joints, Single-lap joint, Cohesive zone models, Stress distributions, Damage analysis.

[1] Corresponding author. Phone:+351939526892; Fax:+351228321159; Email:raulcampilho@gmail.com

1 – Introduction

The joints are always potential loci of damage initiation and, thus, it becomes highly relevant to reduce the number of joints in a structure as well as an efficient design [1]. Fastening is a simple joining technique, but the fastener holes damage the composite components by breaking the fibre continuity and introduce local damage, which affects the structures' strength. Adhesive bonding is a permanent process that uses an adhesive to bond the components of a structure. This bonding process is used to fabricate structures of complex shape that could not be manufactured in one piece, to provide a structural bond that ideally should be at least as resistant as the base materials. Adhesive bonding is a particularly attractive bonding method, which enables joining different materials without damage to the parent structures. Other advantages are smaller weight, more uniform stress distributions, water-proofing and prevention of galvanic corrosion [2, 3]. In some cases, this joining technique is the only available solution, such as in thin-walled parts or plates with large thickness variation [4]. Additionally, the joined area extends longer than with rivets or bolts and stresses are more uniform (especially width-wise), which reflects on higher stiffness and strength. On account of this emerging field of application, different studies have been published that analyse the viability of bonded joints between composites and aluminium [5, 6], composites and steel [7], amongst other combinations. A common feature of all these studies is the performance dependence on a careful design, such that the limitations of bonded joints do not compromise the structural efficiency, such as the sensitivity to peel stresses and stress concentrations in general, or even requirement of surface preparation during the assembly [8]. Driven by this fact, several researchers focused on analytical or numerical techniques to predict the joint strength. The early theoretical methods to estimate stress distributions in bonded joints are not the most suitable method of analysis because of neglecting effects such as adherends and adhesives plasticity, large displacements, among others. When facing complex geometries or to compensate for the limitations of theoretical methods, strength prediction methods for adhesively-bonded joints are nowadays based on the FEM [9, 10] and advanced Fracture Mechanics-based techniques [11]. CZM coupled to FEM analyses simulate damage growth within materials or at interfaces between different materials [12, 13]. The resulting predictions are generally accurate since failure is ruled by energetic criteria, and because the behaviour of materials can be modelled by cohesive laws with different shapes, depending on the experimentally observed behaviour. This technique is based on the establishment of traction-separation laws at the failure paths, and require the values of energy release rate in tension and shear (G_n and G_s, respectively) and respective critical values or toughness (G_n^c and G_s^c). The cohesive strengths in tension and shear (t_n^0 and t_s^0, respectively) are other

required parameters and pertain to damage initiation in the CZM laws. Numerical methods permit the structural analysis of complex shapes (for which no analytical solutions are available) and with complex geometrical and material models. With this, extensive experimentation for design validation can be greatly reduced, with advantages in the design cost and time to accomplishment. These techniques, supported by auxiliary works regarding design rules [14], comparative analyses between different adhesive types [15, 16] and geometrical modifications to reduce stress concentrations [17], should be able to turn adhesive bonding into a highly viable tool in the fabrication of multi-material structures. During the design process, the suitability of this technique should be accompanied by technical and economic considerations [2, 18].

Owens and Lee-Sullivan [19, 20] addressed the stiffness behavior of hybrid composite/aluminium joints, and developed an analytical model to predict the joint stiffness and respective loss with the crack growth. Flexible adhesives were found to increase the resistance to crack growth, thus increasing the joints' strength. Arenas et al. [2] addressed design variables such as the adhesive selection and surface treatment for the adherends in hybrid composite/aluminium joints by experimental testing and an optimization procedure based on multi-criteria decision tools (the analytical hierarchy process – AHP). As a result, it was possible to achieve a parameter combination that combines high joint strength and feasibility in the production process (e.g. time to adhesive preparation, safety or costs). The set of conditions comprised two adhesives (epoxy and polyurethane) and six surface preparation techniques for bonding. Based on the decision tool, the polyurethane adhesive in conjunction with peel-ply and sandpapering treatments for the composite and aluminium adherends, respectively, proved to be the optimal solution. Seong et al. [1] studied the effects of bonding pressure, overlap length (L_O), adherend thickness (t_P) and adherend type on the strength of composite-to-aluminium single-lap joints. One of the main findings was related to the existence of a limiting value of L_O above which the joint strength was left practically constant due to the limited ductility of the adhesive. In the work of Di Franco et al. [21], a systematic experimental study was conducted regarding bonded and hybrid bonded/self-piercing riveted joints between composites and an aluminium alloy. Guidelines were proposed for bonded joint design. It was found that adding a self-piercing rivet to the bonded joint increased the load bearing capabilities of the joint, namely tensile strength, stiffness and energy absorption. Kweon et al. [5] tested double-lap composite-to-aluminium joints considering adhesive bonding, mechanical fastening and hybrid joints. Hybrid joining improved the strength only when mechanical fastening was stronger than adhesive bonding. Other experimental topics include the

cryogenic performance of composite-to-aluminium joints [22], digital image correlation applied to strain measurement [23] or thermal stresses [24]. Rudawska [4] conducted a series of tests and CZM simulations of hybrid joints between different adherend materials (titanium and aluminium alloys and aramid-epoxy composites). The technique was accurate, with the maximum deviation (17%) for the titanium-titanium joints. The hybrid joints showed varying results depending of the chosen adherend combinations, with the best results being found for the aluminium-aluminium joints. Anyfantis [25] studied by CZM modelling and experimentation double-lap joints between Carbon-fibre reinforced plastic (CFRP) composites and steel bonded with a ductile adhesive layer. The elasto-plastic loading and fracture response were modelled by a recently developed mixed-mode CZM law. A comparison was also performed to a numerical analysis based on the Damage Zone Theory (DZT). After validation of the CZM approach, which showed more accurate results than the DZT, a parametric study on the value of L_O was conducted. The increase of L_O showed to concentrate stresses in a smaller portion of the overlap, resulting in a non-linear strength improvement with this parameter. Other authors [26] used the CZM technique to model environmental degradation in composite-to-aluminium joints. Composite-to-aluminium bonded joints under a pure tensile loading were investigated by Khoshravan and Mehrabadi [27] by experiments and FEM modelling, using the Virtual Crack Closure Technique.

This work addresses numerically and experimentally adhesive joints between aluminium and carbon-epoxy components, considering different adhesives and geometric conditions. The strength and failure modes are studied, enabling the optimization of the geometry and material parameters of the joints. Numerically, the FEM is used to perform detailed stress and damage analyses allowing to explain the joints' behaviour. The use of CZM enables predicting the joint strength and creating a simple and rapid design methodology.

2 – Experimental work

2.1 – Materials characterization

Unidirectional carbon-epoxy pre-preg (SEAL® Texipreg HS 160 RM; Legnano, Italy) with 0.15 mm ply thickness was considered for the composite adherends of the single-lap joints, with the $[0]_{20}$ lay-up. Table 1 presents the elastic properties of a unidirectional lamina, modelled as elastic orthotropic in the FEM analysis [28]. Table 2 shows the interlaminar and intralaminar cohesive properties of the pre-preg SEAL® Texipreg HS 160 RM, to be used in the CZM simulations. The adherends were fabricated by hand lay-up followed by curing

in a hot-plates press with the supplier-recommended heat and pressure cycle. The aluminium adherends are made of a laminated high-strength aluminium alloy sheet (AA6082 T651) cut by precision disc cutting into specimens of 140×25×3 mm^3. The mechanical properties of this material are characterized in the literature [11], giving the following bulk values: Young's modulus (E) of 70.07±0.83 GPa, tensile yield stress (σ_y) of 261.67±7.65 MPa, tensile failure strength (σ_f) of 324±0.16 MPa and tensile failure strain (ε_f) of 21.70±4.24%. Two adhesive systems from Nagase ChemteX were evaluated for the hybrid joints: the XNR6823 and the XNR6852. Due to their contrasting mechanical properties, the former is also addressed as brittle and the latter as ductile. These two adhesives were chosen to promote different failure modes in the hybrid joints and, thus, to test the numerical models under different circumstances. The adhesives were characterized regarding the elastic moduli in tension and shear (E and G, respectively), the failure strengths in tension and shear (corresponding to t_n^0 and t_s^0) and the values of G_n^c and G_s^c. Bulk tests were performed to characterize the adhesives in tension and Thick Adherend Shear Tests (TAST) were chosen for shear characterization. Although the cohesive strengths of thin adhesive layers and the bulk strengths of adhesives can differ, since thin layers are constrained between the two adherends and damage growth occurs under mixed-mode [29], in this work the cohesive strengths of the adhesives were assumed as equal to their bulk quantities as an approximation. The authors estimated the values of G_n^c and G_s^c by Double-Cantilever Beam (DCB) and End-Notched Flexure (ENF) tests, respectively, using a robust data reduction method that does not require crack length measurement [30, 31]. The relevant mechanical properties of these adhesives, which were used to construct the cohesive laws, are summarized in Table 3. The large difference between G_n^c and G_s^c observed in Table 3 for the XNR6852 is typical of ductile structural adhesives, which show a significantly larger plastic flow in shear than in tension [32].

2.2 – Joint dimensions, fabrication and testing

Fig. 1 shows a schematic representation and dimensions of the single-lap joints. The considered dimensions are (in mm): L_O=10, 20, 30 and 40, width b=25, specimen length L_T=180, t_P=3 and adhesive thickness t_A=0.2. The joints' fabrication involved manual roughening of the bonding surfaces and cleaning with a degreaser, adherend positioning, adhesive application in a steel mould and removal of the excess adhesive after curing by precision milling. During the assembly, the value of t_A was attained by using a dummy adherend and a 0.2 mm calibrated spacer under the upper adherend. Additionally, in this process, tabs were glued at the specimens' edges to remove gripping misalignments during testing. The XNR6823 was cured at 70ºC for 4 h and the XNR6852 at

150ºC for 3h, in both cases following the data sheet of the adhesives. Joint testing under tension was carried out in an Instron® 4208 (Norwood, MA, USA) electro-mechanical testing machine with a 100 kN load cell, at room temperature and under displacement control (0.5 mm/min). The machine grips displacement and measured load were the output data from the tests, providing the load-displacement (P-δ) curves for all specimens. Five repetitions were tested for each joint configuration.

3 – Numerical work

3.1 – Modelling conditions

The numerical models with CZM capabilities were built in Abaqus® to perform the stress and damage variable analyses, and also for strength prediction. This analysis aims at presenting a detailed discussion of the joints behaviour and comparative evaluation between different adhesives/values of L_O based on the mentioned information, to provide design principles for hybrid joint design. A two-dimensional and geometrically non-linear analysis was considered [11]. The composite and aluminium adherends were modelled as elastic orthotropic (properties given in Table 1) and elastic-plastic isotropic, respectively. The models were built with 4-node plane-strain elements for the adherends and either identical elements for the adhesive layer (stress analysis) or 4-node cohesive elements for the adhesive layer and to simulate a composite failure at a specific distance to the adhesive/composite interface (damage and strength analyses) [32]. The constructed meshes were different between the stress and strength analyses, with the former having a higher degree of refinement to accurately account for stress variations along the joint. In both cases, mesh grading was applied, with a higher refinement near the overlap edges and in the adherends in the direction of the adhesive to account for the expected stress variations. Between different L_O values, to provide identical modelling conditions, the FE elements size in all models was fixed at the overlap edges (0.02×0.02 mm elements for the stress analysis and 0.2×0.2 mm elements for the strength analysis). Fig. 2 shows an example of FE mesh for L_O=10 mm, including mesh details for the stress and strength analyses. Boundary conditions consisted of clamping the joints at one of the edges, and tensile pulling together with transverse restraining at the opposite edge (Fig. 1). The adhesive layer was modelled by CZM elements with a row of cohesive elements [11], and the possibility of composite interlaminar and intralaminar failures was included in the numerical models by a CZM propagation path located at a distance of 0.15 and 0.05 mm, respectively, from the adhesive layer/composite interface. The triangular CZM technique applied in this study is implemented in Abaqus® CAE and is briefly discussed in the following Section.

3.2 – CZM model

CZM are based on a relationship between stresses and relative displacements connecting homologous nodes of the cohesive elements (Fig. 3), to simulate the elastic behaviour up to a peak load and subsequent softening, to model the gradual degradation of material properties up to complete failure. The areas under the traction-separation laws in each mode of loading (tension and shear) are equalled to the respective critical value (G_n^c or G_s^c). Under pure mode, damage propagation occurs at a specific integration point when the stresses are released in the respective traction-separation law. Under mixed mode, energetic criteria are often used to combine tension and shear [33]. The traction-separation law assumes an initial linear elastic behaviour followed by linear evolution of damage. The elastic behaviour of the cohesive elements up to the tipping tractions is defined by an elastic constitutive matrix relating stresses and strains across the interface, containing E and G as main parameters. Damage initiation under mixed-mode can be specified by different criteria. In this work, the quadratic nominal stress criterion was considered for the initiation of damage. After the peak value in Fig. 3 is attained (mixed-mode cohesive strength or t_m^0), the material stiffness is degraded. Complete separation is predicted by a linear power law form of the required energies for failure in the pure modes. For full details of the presented model, the reader can refer to reference [11]. The cohesive parameters for interlaminar/intralaminar CFRP failure were previously presented in Table 2. The cohesive parameters of the adhesives were defined from the property characterization tests depicted in Section 2.1 (Table 3), considering the values of t_n^0 and t_s^0 equal to σ_f and τ_f, respectively.

4 – Results and discussion

4.1 – Stress analysis during the elastic behaviour

In this Section, through-thickness normal (σ_y) and shear (τ_{xy}) stress distributions in the elastic regime of the single-lap joints are taken at different planes in the joint for L_O=10 mm and, afterwards, these stresses are compared at the adhesive mid-thickness between the four L_O values considered in this study. Stresses are only presented for the joints bonded with the XNR6852 because of the similar results compared to the other adhesive, on account of identical elastic properties [34]. Fig. 4 and Fig. 5 present σ_y and τ_{xy} stress distributions at different horizontal planes in the joints with L_O=10 mm as a function of x/L_O (x described in Fig. 1), respectively. The considered planes are the following: P1 – in the composite at 0.15 mm from the adhesive interface, P2 – in the composite at 0.05 mm of the adhesive interface, P3 – at the composite/adhesive interface, P4 – at the adhesive

mid-thickness and P5 – at the adhesive/aluminium interface. In these and the following figures, σ_y and τ_{xy} stresses are normalized by τ_{avg} (the average value of τ_{xy} in the adhesive layer for each value of L_O). Moreover, in some figures the *y*-axis is truncated for a clearer visualization of the relevant differences between curves, while the high peak stresses at the stress singularities are also meaningless as they are mesh-dependent.

For both σ_y and τ_{xy} stresses, only the region $-0.2 \leq x/L_O \leq 1$ is shown, since further within the composite these stresses are negligible. σ_y stresses peak at the overlap edges for all considered planes (Fig. 4). In the composite (planes P1 and P2), σ_y stresses are only relevant near the stress singularities (x/L_O=0 and 1) and quickly vanish within the composite. Between all planes, σ_y peak stresses are highest either at plane P3 (x/L_O=0) or at plane P5 (x/L_O=1), i.e., at the stress singularities. However, these differences are only relevant at the overlap edges, with minor variations between planes within the adhesive layer. The analysis of τ_{xy} stresses (Fig. 5) shows corresponding results to σ_y stresses, namely the sites of major stress concentrations, differences between planes and reduced stresses in the composite adherend outside the overlap region. This analysis was extrapolated for all tested L_O values, giving identical results. The documented behaviour is the typical for bonded joints [28], and it should be responsible for cohesive failure in the adhesive, provided that that the composite through-thickness strength is not smaller than that of the adhesive.

σ_y and τ_{xy} stresses at the adhesive mid-thickness for the different L_O values are presented in Fig. 6 (a) and (b), respectively. σ_y stresses are mostly smaller than τ_{avg}, except at the overlap edges. Highly concentrated peaks appear at these locations due to the adherends rotation [35]. σ_y peak stresses increase with L_O, which is known to reduce the joint strength averaged to the bonded area, especially when using brittle adhesives [36]. The ductility of adhesives partly prevents this limitation of bonded joints because it promotes yielding in the adhesive layer. When considering joints between adherends of different stiffness, such as in the present work, different degrees of adherend flexure appear at the overlap edges. Thus, at the rightmost overlap edge, the higher degree of flexure of the more compliant aluminium adherend (compared to the composite) gives σ_y peak stresses with higher magnitude. This should promote damage initiation at this edge rather than at the opposite. τ_{xy} stress distributions have the common profiles for this joint configuration, with a progressive increase from the adhesive layer centre to the overlap edges [35]. This behaviour is related to the increasing longitudinal straining of the adherends from

the free to the opposite overlap edge [37]. The reported L_O effect for σ_y stresses, i.e., increase with this parameter, is also found in τ_{xy} stresses. In fact, the increase of L_O promotes higher transmitted loads and differential straining between adherends, which then reflects on higher τ_{xy} peak stresses [11]. This behaviour, together with that previously documented for σ_y stresses, should lead to a non-improvement of the joint strength with L_O (particularly with brittle adhesives). The use of a ductile adhesive is prone to avoid this limitation of brittle adhesives by promoting failure at a much higher value of τ_{avg} [38]. The un-symmetrical profiles are due to the different stiffness between adherends, which leads to different degrees of differential straining at the overlap edges. At x/L_O=1, in which shear occurs because of the more compliant aluminium adherend (compared to the composite), τ_{xy} peak stresses are higher in magnitude. However, the difference is smaller than for σ_y stresses. The combined behaviour of σ_y and τ_{xy} stresses suggests damage initiation at x/L_O=1.

4.2 – Damage growth analysis

The damage variable SDEG of the triangular mixed-mode CZM law (Fig. 3) gives the stiffness degradation of the cohesive elements, and is discussed in this Section for a detailed assessment of the joints' failure. This variable ranges between SDEG=0 (anywhere in the elastic part of the mixed-mode CZM law) and SDEG=1 (failure of the CZM element). All SDEG plots are considered for $0 \leq x/L_O \leq 1$. Fig. 7 plots the damage variable SDEG when the maximum load (P_m) is attained in the composite at the aforementioned plane P2 for the XNR6823 (a) and at the adhesive mid-thickness (plane P4) for the XNR6852 (b). These planes are consistent with the failure of each type of joints, whilst the other planes, although in some cases entering the softening region (SDEG>0), resulted irrelevant for the joints failure. For the XNR6823 (Fig. 7 a), experiencing composite failure, damage initiates at x/L_O=1 for all L_O values. This is related to the higher magnitude of σ_y and τ_{xy} peak stresses than at x/L_O=0, as depicted in Fig. 6 (a) and (b), respectively. With the increase of L_O, damage in the composite at P_m spans to gradually smaller normalized areas, more specifically 54.1% (L_O=10 mm), 11.6% (L_O=20 mm), 7.2% (L_O=30 mm) and 5.7% (L_O=40 mm), which should be related to a small P_m improvement with the increase of L_O. The behaviour is markedly different for the joints bonded with the XNR6852 (Fig. 7 b), failing by cohesive failure of the adhesive. Despite the SDEG plots being unsymmetrical because of the stress distributions asymmetry (Fig. 6 (a) and (b)), the SDEG curves are practically symmetrical with respect to the middle of the adhesive layer. This is because of the adhesive ductility, which absorbs peak stresses and smoothens stress distributions. The increase of L_O is responsible for an increase of overall damage in the

adhesive layer at the time of failure. Actually, the percentile portion of the overlap under damage for gradually increasing values of L_O from 10 to 40 mm is 73.7%, 86.3%, 96.0% and 97.3%, by the respective order. This behaviour is the opposite of that of the XNR6823, and shows that the adhesive has a large plasticization ability up to L_O=40 mm, showing that the P_m improvement with this adhesive system should be considerable.

The evolution of the damage variable SDEG with δ is described next for both adhesives and L_O=10 and 40 mm, for a better perception of the failure process. Only the limiting values of L_O (10 and 40 mm) are addressed, since the intermediate L_O values show an averaged failure behaviour. The presented curves correspond to different values of $\delta/\delta_{Pmax}\times100$ [%] (δ_{Pmax} is the displacement when P_m is attained). For the joints bonded with the XNR6823, failure took place in the composite (plane P2). Fig. 8 shows the composite failure process for the joints with L_O=10 (a) and 40 mm (b). For L_O=10 mm, failure initiates in the composite at x/L_O=1 and then propagates to the other edge of the overlap. This occurs because of the higher mechanical properties of the adhesive, which make the composite to fail prematurely due to the high stresses involved. The failure process occurs very swiftly up to x/L_O=0 because of the composite brittleness. Actually, complete failure in the overlap is reached with δ/δ_{Pmax}=100.4%. This reinforces the idea of a diminished improvement of P_m with L_O. Considering the joint with L_O=40 mm, the overall behaviour is similar. However, P_m occurs with a much more reduced amount of damage in the composite. Complete overlap failure corresponds to δ/δ_{Pmax}=101%, which is a marginally higher value than for L_O=10 mm. Fig. 9 (a) and (b) presents an identical analysis for the joints bonded with the XNR6852. A significant difference was found for the ductile adhesive, because of its ductility and failure no longer occurring in the composite. The variation of SDEG through the bondline is much more gradual. Considering the instant of δ/δ_{Pmax}=100%, i.e. when P_m is attained, the fraction of the adhesive layer under damage or surpassing the elastic limit is 73.7% (L_O=10 mm) and 96.0% of the overlap (L_O=40 mm). Complete failure for the hybrid joint with L_O=10 mm occurs at $\delta/\delta_{Pmax}\approx$170%, which is a much more gradual failure process than for the XNR6823, and is induced by the adhesive ductility. For L_O=40 mm, failure occurs at $\delta/\delta_{Pmax}\approx$100.22%. This significant reduction of δ/δ_{Pmax} at joint failure is related to the bigger δ value at δ/δ_{Pmax}=100%, induced by the bigger L_O value. The overall behaviour exhibited for the joints bonded with the XNR6852 should be responsible for a significant improvement of P_m with L_O, oppositely to the joints bonded with the XNR6823.

4.3 – Failure mode assessment

In the experiments, the joints bonded with the brittle XNR6823 suffered intralaminar failure of the composite for all L_O values beginning at x/L_O=1, at a measured distance from the composite/adhesive interface of nearly 0.05 mm (thus approximately at plane P2). These results were consistent with the numerical predictions. Fig. 10 gives a comparison of a representative experimental failure (a) and respective numerical prediction (b) for L_O=10 mm. On the other hand, the joints bonded with the ductile XNR6852 showed cohesive failure of the adhesive layer, in close agreement with the numerical simulations (Fig. 11 compares the failure for L_O=10 mm as an example).

4.4 – Joint strength

Fig. 12 (a) and (b) provide the experimental/numerical comparison of P_m vs. L_O for the joints bonded with the XNR6823 and XNR6852, respectively. As previously mentioned, a brittle failure in the composite took place with the XNR6823 (Fig. 12 a). Experimental and numerical failures occurred at plane P2 for all joint configurations, and this is related to the significantly smaller peel and shear mechanical properties of the composite compared to those of the adhesive at plane P4 (Table 2 compared to Table 3), although peak σ_y and τ_{xy} stresses are marginally smaller at plane P2 at x/L_O=1 (Fig. 4 and Fig. 5) when failure initiates. The brittle failure in the composite for the joints bonded with the XNR6823 resulted in a very small P_m improvement with L_O, as it can be testified in both experimental and numerical data. Actually, the P_m improvement for L_O=40 mm over L_O=10 mm was 43.4% (numerical) or 15.6% (experimental), which can be compared to the behaviour or bonded joints when brittle failures in the adhesive layer take place. The damage variable analysis previously presented in Fig. 7 (a) for the damaged state of the composite at plane P2 for these joints shows signs of a brittle intralaminar failure of the composite. In fact, although for L_O=10 mm P_m corresponds to partial degradation of the composite at 54% of L_O, this damaged length significantly reduces up to L_O=40 mm (damaged portion of L_O of only 5.7%). Thus, the composite clearly is not capable of accommodating the peak stresses at the free edge of the adherend, resulting in a brittle failure. The occurrence of a large damage zone for L_O=10 mm, on the other hand, is a result of more uniform stress distributions for short L_O values (Fig. 6) [11]. Fig. 8, showing the evolution of the damage variable with the applied loading, reinforces this assumption, by testifying the quick failure process up to complete joint failure (values of δ/δ_{Pmax} at failure of 100.4% for L_O=10 mm and 101% for L_O=40 mm). This behaviour shows a limited benefit in increasing L_O for these joints.

The joints bonded with the XNR6852 showed a linear increase of P_m vs. L_O (Fig. 12 b). As previously mentioned, these joints failed cohesively in the adhesive layer. This can be explained by the inferior adhesive layer strength properties, compared to those of the XNR6823 (Table 3), promoting premature failure of the adhesive layer with respect to the composite. Although the adhesive properties are still superior to those of the composite (Table 2), failure in the composite was prevented by overall smaller σ_y and τ_{xy} stresses (Fig. 4 and Fig. 5), despite at very localised regions this is not exactly true. Both in the experimental and numerical curves the absence of a limiting value of P_m is noted, which is indicative that the failure strength or at least the yield stress of the CFRP and aluminium adherends was not reached for the obtained P_m values. The stress analysis of Fig. 6 a) (σ_y stresses) and b) (τ_{xy} stresses) showed that both stress components are more uniform along the bond length for small L_O values. However, since the XNR6852 is highly ductile, it enables plasticization of the adhesive layer beginning at the overlap edges when the limiting stresses are attained, and the joints fail after significant plasticization of the adhesive layer [3]. This justifies the nearly linear evolution of P_m with L_O depicted in Fig. 12 b). Another characteristic of this type of behaviour was the abrupt failure of the specimens, without crack growth before P_m, showing that cracking was prevented at the overlap edges up to P_m being reached [39]. The damage variable analyses also corroborate this assumption. Fig. 7 (b) shows that P_m occurs with a significant amount of the adhesive layer under softening (from 73.7% for L_O=10 mm up to 97.3% for L_O=40 mm). This shows that the adhesive layer undergoes extensive plasticization, which reinforces the linear trend in the P_m vs. L_O plots. The evolution of the damage variable with δ/δ_{Pmax} corroborates this fact (Fig. 9), by showing a very gradual evolution of damage and failure under conditions proximal to generalised yielding of the adhesive.

The results of Fig. 12 (a) and (b) show that the CZM technique was accurate in predicting the joints strength, for both failure modes, i.e., cohesive failure of the adhesive layer and intralaminar failure of the composite. The maximum deviation between the experiments and numerical simulations for the joints bonded with the XNR6823, experiencing intralaminar failure in the composite, was 11.2% for L_O=10 mm. The maximum deviation for the joints bonded with the XNR6852, relating to cohesive failure of the adhesive layer, was 8.0% (for L_O=40 mm). In both cases the differences were averaged over the experimental values. The variation observed for the XNR6823 is justified by inherent issues to composite failures, such as larger properties variations, complexity in the failure modes including fibre bridging events, unstable damage growth, amongst

other issues [6]. Nonetheless, the deviation values were quite acceptable. For the XNR6852, the increasing under predictions were clearly caused by the large plastic flow of this adhesive, which is only modelled in an approximated manner by triangular CZM. Despite this fact, the maximum deviation of 8.0% is perfectly acceptable. For more accurate results a trapezoidal cohesive law can be used instead [40].

5 – Concluding remarks

This work aimed at studying, by experimentation and CZM modelling, the tensile behaviour of adhesive joints between aluminium and CFRP adherends, bonded with a brittle and a ductile adhesive and different L_O values. The stress analysis showed that σ_y and τ_{xy} stresses peak at the overlap edges, and that these are highest at the adherends/adhesive interfaces. Stresses between different horizontal planes in the joints are similar, except for some variation in the peak values at the overlap edges. σ_y and τ_{xy} stresses are more uniform for short L_O values and tend to increase stress gradients towards the overlap edges with the increase of L_O. The damage analysis enabled a deeper insight of the joints behaviour, showing a brittle composite fracture occurring for the joints with the brittle adhesive, testified by the short damage length and quick failure process. On the other hand, the joints with the ductile adhesive failed cohesively in the adhesive layer under global yielding conditions, which was corroborated by the large damage length at the instant of P_m. The joints behaviour as a function of L_O was consistent with these analyses, with the joints bonded with the brittle adhesive giving a negligible strength improvement with L_O. The joints bonded with the ductile adhesive showed a nearly linear P_m improvement with L_O, which agrees with the global yielding conditions at failure previously detected in the damage analysis. The joints strength and failure modes were highly dependent on the adhesive type (brittle or ductile), and this behaviour was successfully modelled numerically.

References

1. Seong MS, Kim TH, Nguyen KH, Kweon JH, Choi JH. A parametric study on the failure of bonded single-lap joints of carbon composite and aluminium. Composite Structures 2008;86:135-145.
2. Arenas JM, Alía C, Narbón JJ, Ocaña R, González C. Considerations for the industrial application of structural adhesive joints in the aluminium-composite material bonding. Composites: Part B 2013;44:417-423.

3. Adams RD, Comyn J, Wake WC. Structural Adhesive Joints in Engineering, 2nd ed. London: Chapman & Hall, 1997.
4. Rudawska A. Adhesive joint strength of hybrid assemblies: Titanium sheet-composites and aluminium sheet-composites – Experimental and numerical verification. International Journal of Adhesion & Adhesives 2010;30:574-582.
5. Kweon JH, Jung JW, Kim TH, Choi JH, Kim DH. Failure of carbon composite-to-aluminium joints with combined mechanical fastening and adhesive bonding. Composite Structures 2006;75:192-198.
6. Kim TH, Kweon JH, Choi JH. An experimental study on the effect of overlap length on the failure of composite-to-aluminium single-lap bonded joints. Journal of Reinforced Plastics and Composites 2008;27:1070-1081.
7. Osnes H, McGeorge D. Experimental and analytical strength analysis of double-lap joints for marine application. Composites: Part B 2009;40:29-40.
8. LeBack C, Brechet Y, Shercliff HR, Jeggy T, Salvo L. Selection of joining methods in mechanical design. Materials & Design 2002;23:405-416.
9. Zadpoor AA, Sinke J, Benedictus R. The mechanical behavior of adhesively bonded tailor-made blanks International Journal of Adhesion & Adhesives 2009;29:558-571.
10. Andreassi L, Baudille R, Biancolini ME. Spew formation in a single lap joint. International Journal of Adhesives & Adhesives 2007;27:458-468.
11. Campilho RDSG, Banea MD, Pinto AMG, da Silva LFM, de Jesus AMP. Strength prediction of single- and double-lap joints by standard and extended finite element modelling. International Journal of Adhesion & Adhesives 2011;31:363-372.
12. da Silva LFM, Campilho RDSG. Advances in Numerical Modelling of Adhesive Joints. Heidelberg: Springer, 2012.
13. Feraren P, Jensen HM. Cohesive zone modelling of interface fracture near flaws in adhesive joints. Engineering Fracture Mechanics 2004;71:2125-2142.
14. Van Straalen IJJ, Wardenier J, Vogelesang LB, Soetens F. Structural adhesive joints in engineering-drafting design rules. International Journal of Adhesion & Adhesives 1998;18:41-49.
15. Edwards KL. A brief insight into the selection and use of engineering adhesives for preliminary joint design. Materials & Design 1998;19:121-123.

16. Fernandes TAB, Campilho RDSG, Banea MD, da Silva LFM. Adhesive selection for single lap bonded joints: experimentation and advanced techniques for strength prediction. The Journal of Adhesion, in press.
17. Campilho RDSG, de Moura MFSF, Domingues JJMS. Numerical prediction on the tensile residual strength of repaired CFRP under different geometric changes. International Journal of Adhesion and Adhesives 2009;29:195-205.
18. Arenas JM, Narbón JJ, Alía C. Influence of the surface finish on the shear strength of structural adhesive joints and application criteria in manufacturing processes. The Journal of Adhesion 2009;85:324-340.
19. Owens JFP, Lee-Sullivan P. Stiffness behaviour due to fracture in adhesively bonded composite-to-aluminum joints I. Theoretical model. International Journal of Adhesion and Adhesives 2000;20:39-45.
20. Owens JFP, Lee-Sullivan P. Stiffness behavior due to fracture in adhesively bonded composite-to-aluminum joints II. Experimental. International Journal of Adhesion and Adhesives 2000;20:47-58.
21. Di Franco G, Fratini L, Pasta A. Analysis of the mechanical performance of hybrid (SPR/bonded) single-lap joints between CFRP panels and aluminium blanks. International Journal of Adhesion & Adhesives 2013;41:24-32.
22. Kang SG, Kim MG, Kim CG. Evaluation of cryogenic performance of adhesives using composite-aluminium double-lap joints. Composite Structures 2007;78:440-446.
23. Moutrille MP, Derrien K, Baptiste D, Balandraud X, Grédiac M. Through-thickness strain field measurement in a composite/aluminium adhesive joint. Composites: Part A 2009;40:985-996.
24. Rastogi N, Soni SR, Nagar A. Thermal stresses in aluminium-to-composite double-lap bonded joints. Advances in Engineering Software 1998;29:273-281.
25. Anyfantis KN. Finite element predictions of composite-to-metal bonded joints with ductile adhesive materials. Composite Structures 2012;94:2632-2639.
26. Liljedahl CDM, Crocombe AD, Wahab MA, Ashcroft IA. Modelling the environmental degradation of adhesively bonded aluminium and composite joints using a CZM approach. International Journal of Adhesion & Adhesives 2007;27:505-518.
27. Khoshravan M, Mehrabadi FA. Fracture analysis in adhesive composite material/aluminium joints under mode-I loading: experimental and numerical approaches. International Journal of Adhesion & Adhesives 2012;39:8-14.

28. Campilho RDSG, de Moura MFSF, Domingues JJMS. Modelling single and double-lap repairs on composite materials. Composites Science and Technology 2005;65:1948-1958.
29. Ji G, Ouyang Z, Li G, Ibekwe S, Pang SS. Effects of adhesive thickness on global and local Mode-I interfacial fracture of bonded joints. International Journal of Solids and Structures 2010;47:2445-2458.
30. de Moura MFSF, Campilho RDSG, Gonçalves JPM. Crack Equivalent Concept Applied to the Fracture Characterization of Bonded Joints under Pure Mode I Loading. Composites Science and Technology 2008;68:2224-2230.
31. de Moura MFSF, Campilho RDSG, Gonçalves JPM. Pure mode II fracture characterization of composite bonded joints. International Journal of Solids and Structures 2009;46:1589-1595.
32. Neto JABP, Campilho RDSG, da Silva LFM. Parametric study of adhesive joints with composites. International Journal of Adhesion & Adhesives 2012;37:96-101.
33. Ridha M, Tan VBC, Tay TE. Traction-separation laws for progressive failure of a bonded scarf repair of composite panel. Composite Structures 2011;93:1239-1245.
34. Adams RD. Adhesive Bonding: Science, Technology and Applications. Woodhead Publishing Ltd, Bristol, 2005.
35. Zhao B, Lu ZH, Lu YN. Two-dimensional analytical solution of elastic stresses for balanced single-lap joints – Variational method. International Journal of Adhesion & Adhesives 2014;49:115-126.
36. Reis P, Antunes F, Ferreira JAM. Influence of superposition length on mechanical resistance of single lap adhesive joints. Composite Structures 2005;67:125-133.
37. Jiang W, Qiao P. An improved four-parameter model with consideration of Poisson's effect on stress analysis of adhesive joints. Engineering Structures 2015;88:203-215.
38. da Silva LFM, Carbas RJC, Critchlow GW, Figueiredo MAV, Brown K. Effect of material, geometry, surface treatment and environment on the shear strength of single lap joints. International Journal of Adhesion & Adhesives 2009;29:621-632.
39. Hu FZ, Soutis C. Strength prediction of patch repaired CFRP laminates loaded in compression. Composites Science and Technology 2000;60:1103-1114.
40. Campilho RDSG, Banea MD, Neto JABP, da Silva LFM. Modelling adhesive joints with cohesive zone models: effect of the cohesive law shape of the adhesive layer. International Journal of Adhesion & Adhesives 2013;44:48-56.

Figures

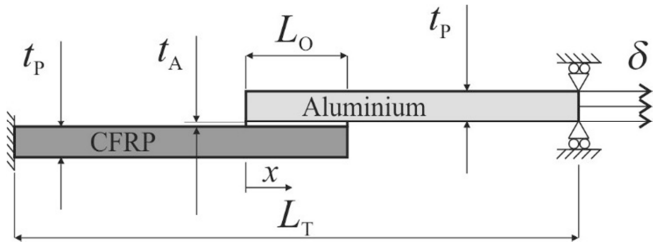

Fig. 1 – Geometry and characteristic dimensions of the single-lap joints.

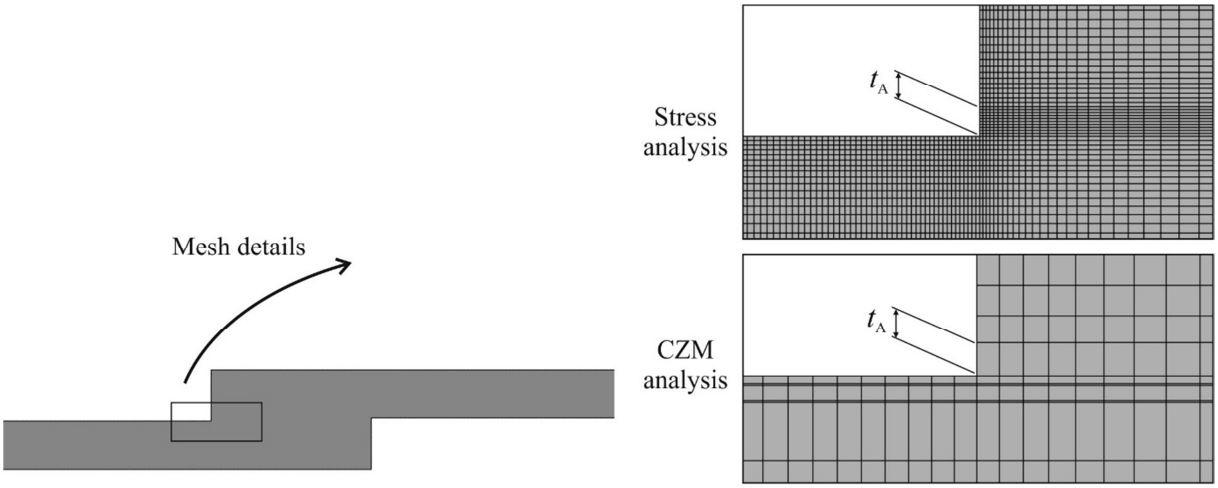

a) b)

Fig. 2 – Example of FEM mesh for L_O=10 mm, including mesh details for the stress and damage analyses.

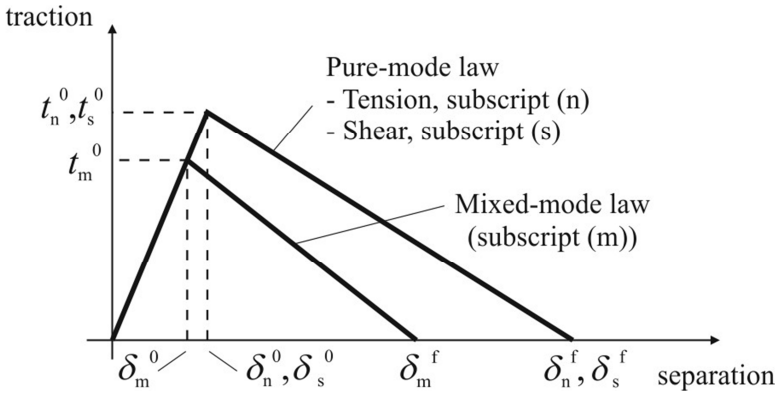

Fig. 3 – Traction-separation law with linear softening law available in Abaqus®.

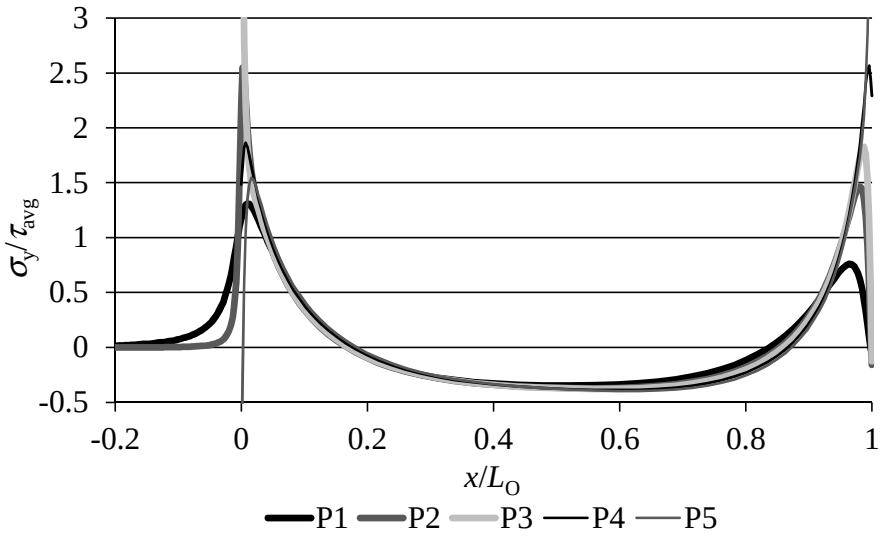

Fig. 4 – σ_y stress distributions at the different planes in the joints' height for L_O=10 mm.

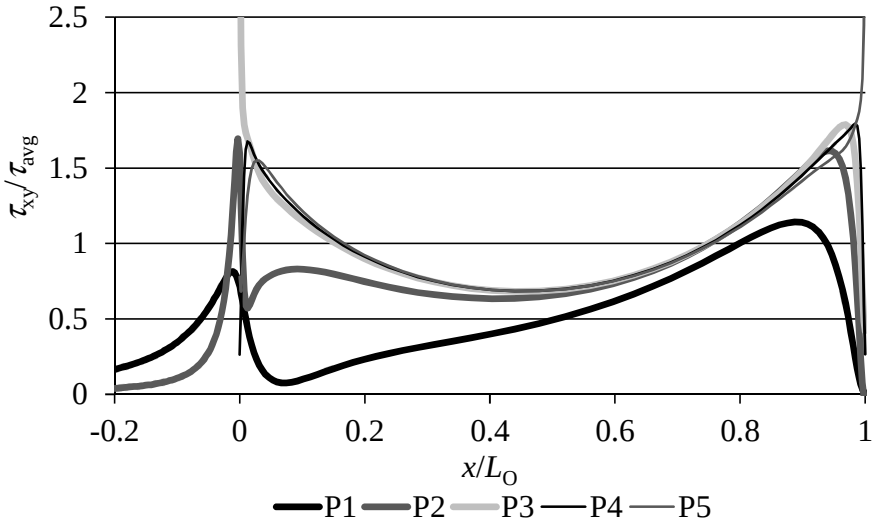

Fig. 5 – τ_{xy} stress distributions at the different planes in the joints' height for L_O=10 mm.

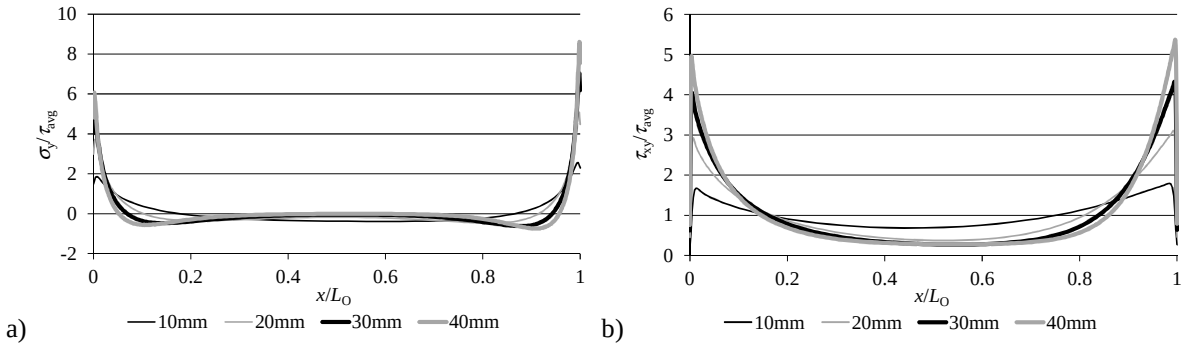

Fig. 6 – σ_y (a) and τ_{xy} (b) stress distributions at the adhesive mid-thickness as a function of L_O.

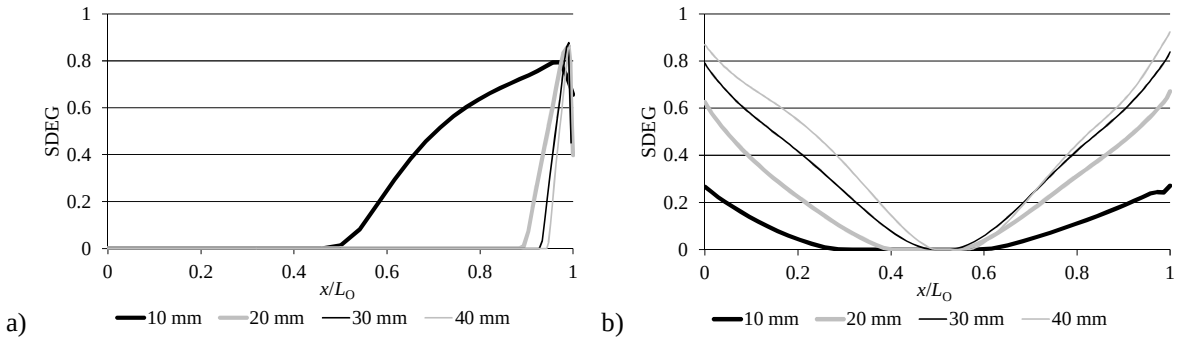

Fig. 7 – Damage variable across plane P2 at P_m for the joints bonded with the XNR6823 (a) and across plane P4 for the joints bonded with the XNR6852 (b).

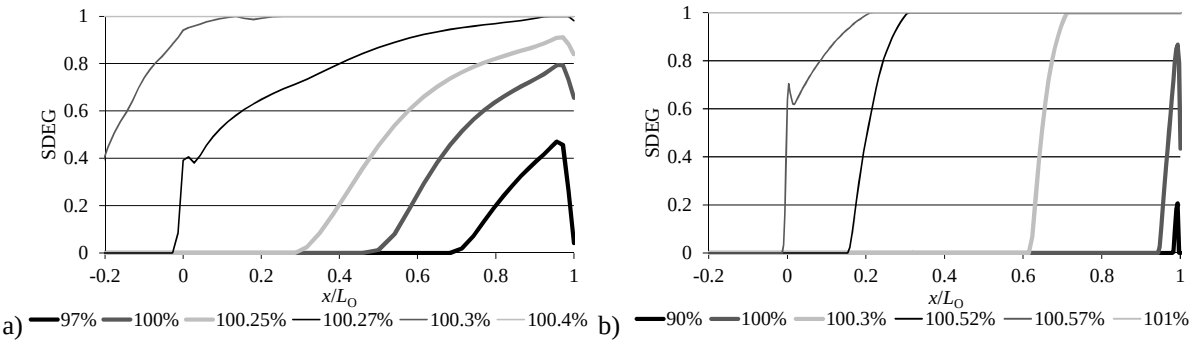

Fig. 8 – Evolution of the damage variable SDEG across the composite (plane P2) with increasing values of δ/δ_{Pmax} for the hybrid joints bonded with the XNR6823 and L_O=10 mm (a) and L_O=40 mm (b).

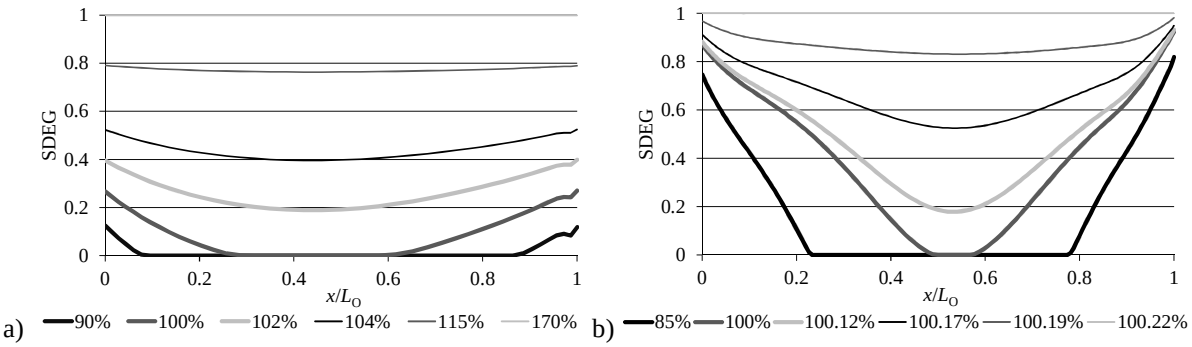

Fig. 9 – Evolution of the damage variable SDEG across the bondline (plane P4) with increasing values of δ/δ_{Pmax} for the hybrid joints bonded with the XNR6852 and L_O=10 mm (a) and L_O=40 mm (b).

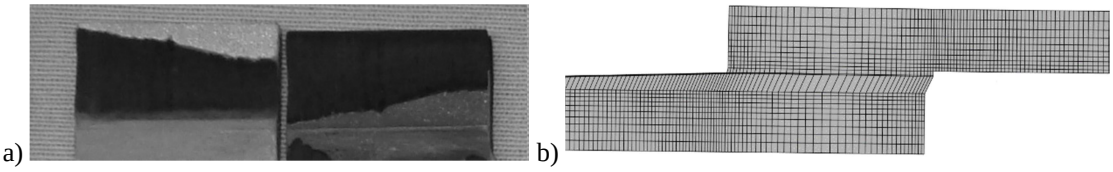

Fig. 10 – Representative experimental failure (a) and respective numerical prediction (b) for the joints with XNR6823 and L_O=10 mm.

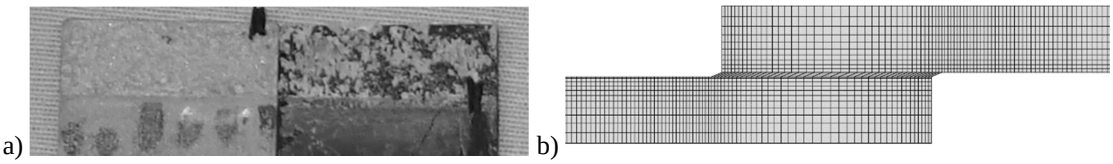

Fig. 11 – Representative experimental failure (a) and respective numerical prediction (b) for the joints with XNR6852 and L_O=10 mm.

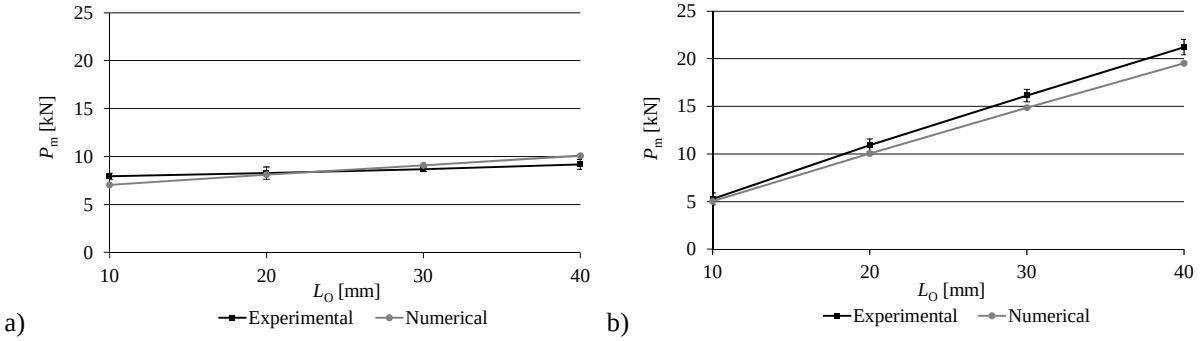

Fig. 12 – Experimental and numerical values of P_m vs. L_O for the joints bonded with the adhesive XNR6823 (a) and XNR6852 (b).

Tables

Table 1 –Elastic orthotropic properties of a unidirectional carbon-epoxy ply aligned in the fibres direction (*x*-direction; *y* and *z* are the transverse and through-thickness directions, respectively) [28].

E_x=1.09E+05 MPa	ν_{xy}=0.342	G_{xy}=4315 MPa
E_y=8819 MPa	ν_{xz}=0.342	G_{xz}=4315 MPa
E_z=8819 MPa	ν_{yz}=0.380	G_{yz}=3200 MPa

Table 2 – Interlaminar and intralaminar cohesive properties of the pre-preg SEAL® Texipreg HS 160 RM.

Property	
Tensile stiffness, K_1 [N/mm^3]	10^6
Tensile cohesive strength, t_n^0 [MPa]	25.0
Shear stiffness, K_2 [N/mm^3]	10^6
Shear cohesive strength, t_s^0 [MPa]	25.0
Toughness in tension, G_n^c [N/mm]	0.18
Toughness in shear, G_s^c [N/mm]	0.5

Table 3 – Relevant properties of the adhesives XNR6823 and XNR6852.

Property	**XNR6823**	**XNR6852**
Young's modulus, E [MPa]	2600	2235.5
Tensile failure strength, σ_f [MPa]	57	48
Shear modulus, G [MPa]	1000	859.8
Shear failure strength, τ_f [MPa]	32.9	20.5
Toughness in tension, G_n^c [N/mm]	1.18	2.0
Toughness in shear, G_s^c [N/mm]	1.5	4.4